PAPER

Multifunctional protein-based self-assembled nanoplatform: overcoming hypoxic tumor microenvironment for enhanced imaging-guided photodynamic therapy†

Min Li,‡[a,b] Ziyi Cheng, [ID] ‡[a,b] Heng Liu,[a,b] Kun Dou,[a,b] Huan Xiao,*[a,c] Linlu Zhao [ID] *[a,b] and Fabiao Yu [ID] *[a,b]

Photodynamic therapy (PDT) has emerged as a promising modality for cancer treatment, but its efficacy is often limited by tumour hypoxia. Here, we report the development of a novel protein-based, self-assembled nanoplatform, CAT-I-BODIPY NPs (CIB NPs), to address this limitation. We first design and synthesize an I-BODIPY photosensitizer based on the heavy atom effect and modification of the electron-donating group, which exhibits excellent capabilities in generating reactive oxygen species and enabling near-infrared (NIR) fluorescence imaging. The incorporation of an oxygen-producing enzyme, catalase (CAT), within these nanoassemblies enables *in situ* oxygen generation to counteract hypoxic constraints. Controllable self-assembly by multiple supramolecular interactions into highly ordered architecture not only guarantees CAT's catalytic activity but also leads to excellent NIR fluorescence imaging ability and enhanced PDT efficacy. Notably, the visualization of optimal accumulation of CIB NPs within tumour sites 18 h post-injection offers precise PDT application guidance. Both *in vitro* and *in vivo* studies corroborate the remarkable anti-tumour efficacy of CIB NPs under NIR illumination, providing a significant advancement in PDT. The favourable biosafety profile of CIB NPs further emphasizes their potential for clinical application in hypoxic tumour therapy.

1. Introduction

The annual increase in cancer mortality has placed a tremendous burden on modern society, which necessitates the urgent development of innovative cancer therapies.[1–3] Photodynamic therapy (PDT) has emerged as a promising cancer treatment modality with significant advantages, such as minimal invasiveness, low toxicity, negligible drug resistance, and excellent spatiotemporal selectivity.[4–8] Among various photosensitizers (PSs) utilized for PDT, boron dipyrromethene (BODIPY) derivatives have attracted considerable attention due to their superior photochemical properties and potential as dual-function agents for both bioimaging and PDT.[9–14] Particularly, the introduction of heavy atom iodine to BODIPY significantly enhances the photodynamic effect, mainly attributed to the heavy-atom effect, which improves spin–orbital coupling and facilitates the intersystem crossing rate, thus increasing the $^1O_2$ QYs of PSs.[15,16] Simultaneously, identifying the optimal treatment window is vital in phototherapy, as fluorescence imaging techniques allow for the visualization of the phototherapeutic process due to their high sensitivity, real-time monitoring capabilities, and noninvasive nature.[17–20] Remarkably, iodinated BODIPY candidates also maintain satisfactory fluorescence imaging properties, making them suitable for imaging-guided PDT.[16,21,22] Nevertheless, for these type I PSs, oxygen supply is essential to guarantee effective PDT, which may be restricted due to the intrinsically hypoxic tumour microenvironment.[23–25] Furthermore, the inherent hydrophobicity of BODIPY easily leads to molecular aggregation, resulting in reduced therapeutic outcomes.[26] To address these challenges and boost the selectivity and efficiency of PDT, there is an urgent need for the development of innovative PSs and strategies.[27]

The emergence of supramolecular self-assembly nanotechnology has provided an opportunity to propel the further

[a] The First Affiliated Hospital of Hainan Medical University, Hainan Medical University, Haikou 571199, China.
E-mail: zhaolinlu@hainmc.edu.cn, yufabiao@hainmc.edu.cn, xiaohuan1164@163.com
[b] Engineering Research Center for Hainan Bio-Smart Materials and Bio-Medical Devices, College of Emergency and Trauma, Hainan Medical University, Haikou 571199, China
[c] The First Affiliated Hospital of Xi'an Jiaotong University, Xi'an 710061, China
†Electronic supplementary information (ESI) available: Detailed experimental procedures, and supporting figures. See DOI: https://doi.org/10.1039/d3bm01130e
‡These authors contributed equally to this work.

development of efficient PDT.[28–30] Through the orderly arrangement of various components, it can not only achieve multifunctional integration in one platform with increased stability but also allows for enhanced control over the physicochemical properties of the assembled nanostructures, thus improving therapeutic efficacy.[31] To tackle tumour hypoxia, various strategies have been explored, including direct oxygen supply, enhancing intratumoral blood flow, and *in situ* oxygen production.[32,33] Catalase (CAT), a natural enzyme with excellent biocompatibility, is an ideal choice for oxygen supply in tumours due to its ability to generate oxygen from hydrogen peroxide (H_2O_2).[34–37] However, most studies focus on modifying CAT, which may compromise its efficiency and oxygen-generating ability.[35,36] On the other hand, direct binding of functional moieties is more advantageous for improving the biosafety of the nanosystem compared to traditional encapsulation.[38] Therefore, it is crucial to develop suitable strategies that effectively integrate proteins and PSs for safe and efficient tumor treatment.[39,40]

In this study, we developed a protein-based self-assembled nanoplatform (CAT-I-BODIPY NPs) for enhanced PDT of hypoxic tumours. The intriguing I-BODIPY PS, with remarkable ROS-generating ability and NIR-emissive fluorescence imaging capability, was synthesized by introducing heavy atom iodine and an electron-donating group 4-methoxybenzaldehyde. Oxygen-producing CAT with inherent biocompatibility was integrated into the nanoplatform to overcome hypoxic tumour microenvironments. Upon rational design and regulation of hydrophobic and hydrogen-bonding interactions, the self-assembly of CAT and I-BODIPY could be conducted to construct highly ordered nanoarchitectures. Under NIR laser irradiation, the real-time visualization by fluorescence imaging allowed for guiding the optimal time window for treatment. The ordered assembly of multi candidates well guaranteed the integration and functional maximization of each motif. Furthermore, the *in situ* oxygen generation of the nanoassemblies led to a significant promotion of the photodynamic effect and efficient cancer cell apoptosis. The innovative CAT-I-BODIPY nanoplatform addressed conventional PS limitations, providing a promising and biocompatible strategy for non-invasive hypoxic tumour treatment (Scheme 1).

2. Experimental section

2.1 Materials and reagents

All reagents purchased from commercial sources were used without further purification. The 3-bromopropyne and anisic aldehyde were purchased from Anhui Zesheng Technology Co., Ltd. The 2,3-dichloro-5,6-dicyano-*p*-benzoquinone, 4-hydroxy benzaldehyde, and boron trifluoride diethyl etherate were purchased from Shanghai Aladdin Biochemical Technology Co., Ltd. The sodium thiosulfate solution was obtained from Shanghai Acmec Biochemical Co., Ltd. Chloroform-D was purchased from Shanghai Titan Technology Co., Ltd. Trifluoroacetic acid (TFA) was obtained from Shanghai
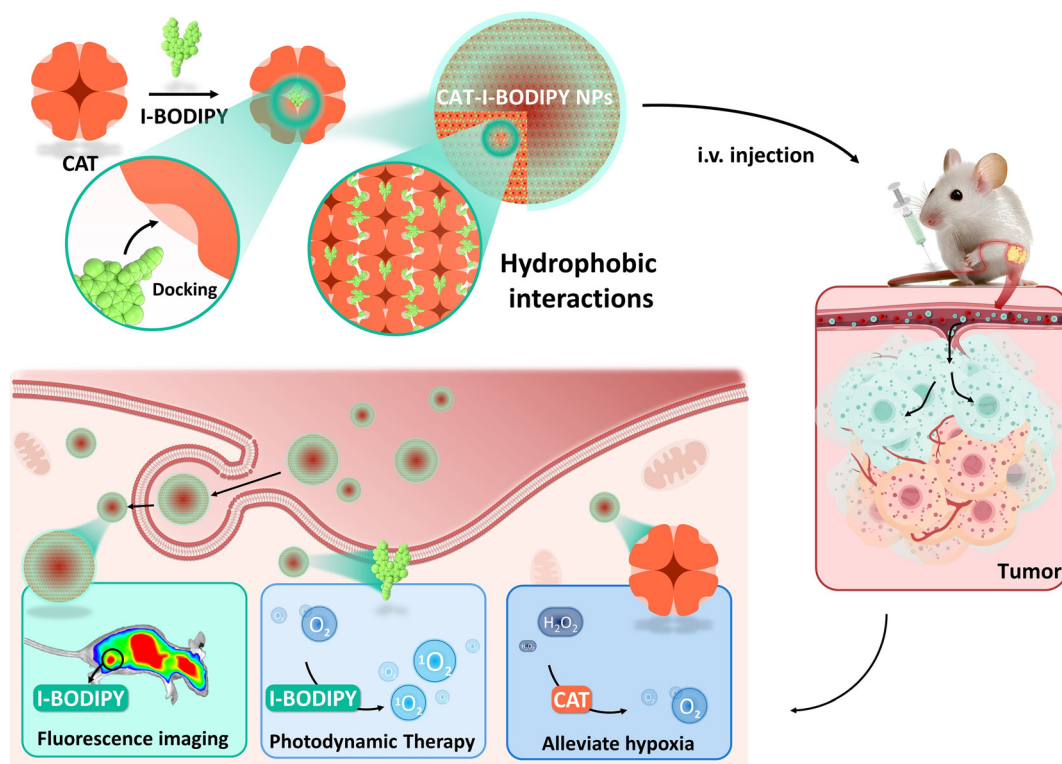
Scheme 1 The self-assembled nanomaterials of CAT and I-BODIPY with *in situ* oxygen-supplementation for enhanced PDT.

Macklin Biochemical Co., Ltd. Iodine, iodic acid, and 2,4-dimethylpyrrole were purchased from the Energy Chemical. The Phosphate Buffered Saline (PBS) Instant Premixed Granules were obtained from Shanghai Ruiyue Experimental Equipment Co., Ltd. Toluene, triethylamine, *n*-hexane, petroleum ether, soda lime, sodium chloride, ethyl acetate, dichloromethane, ethanol, sodium sulfate anhydrous, potassium carbonate anhydrous, dimethyl sulfoxide, acetic acid, *N,N*-dimethylformamide, potassium dihydrogen phosphate, di-potassium hydrogen phosphate trihydrate, and hydrogen peroxide 30% were purchased from Xilong Chemical Co., Ltd. Piperidine was obtained from China National Pharmaceutical Group Co., Ltd. Acetone was purchased from Guangzhou Chemical Reagent Factory, and DMSO (dimethyl sulfoxide) was obtained from Beijing Soleil Technology Co., Ltd. The A549 cell line, 4T1 cell line, and Ham's F-12K basal culture medium were purchased from Procell Life Science & Technology Co., Ltd. The Cell Counting Kit-8 (CCK-8) was obtained from Shanghai BestBio Biotechnology Co., Ltd. The cell digestion trypsin and RPMI Medium 1640 culture medium were purchased from Thermo Fisher Scientific (China) Co., Ltd. Fetal bovine serum was obtained from Sigma Aldrich (Shanghai) Trading Co., Ltd. The triple antibiotics (penicillin–streptomycin–neomycin solution) were purchased from Absin Bioscience (Shanghai) Co., Ltd. The Calcein-AM/PI cell viability and cytotoxicity assay kit were purchased from Shanghai Biyuntian Biotechnology Co., Ltd. Isoflurane was obtained from Shanghai Yuyan Scientific Instrument Co., Ltd. The ^{60}Co irradiation disinfection pads were purchased from Hunan SJA Laboratory Animal Co., Ltd. SPF grade experimental animal feed was obtained from Guangdong Medical Laboratory Animal Center.

2.2 Instruments

The ^{1}H NMR experiments were carried out using a nuclear magnetic resonance (NMR) spectrometer (JNM-ECZ400S/L1, JEOL, Japan). TOF-MS experiments were performed using an ultra-high-performance liquid chromatography quadrupole time-of-flight mass spectrometer (Xevo G2-XS QTOF, Waters, USA). Ultrapure water used in the experiments was prepared using an ultrapure water system (WP-UP-YJ-30, Waterproof, China). Fluorescence spectra and UV-vis absorption spectra were obtained using a fluorescence spectrophotometer (F-4600, Hitachi, Japan) and a UV-vis spectrophotometer (U-2910, Hitachi, Japan), respectively. The morphology and size of CIB NPs were observed using a transmission electron microscope (HT-7800, Hitachi, Japan). The particle size distribution of CIB NPs was measured using a dynamic light scattering instrument (SZ-100Z2/*, HORIBA, Japan). The oxygen content of the solution was determined using a portable dissolved oxygen meter (Mettler Multi InLab®OptiOx, METTLER TOLEDO, Switzerland). In the CCK-8 assay, the absorbance of formazan was measured with a microplate reader (Synergy H1, Biotek, USA). Laser confocal scanning microscopy (FV3000, Olympus, Japan) was used for cell imaging experiments. Flow cytometry (FACSAria, BD) was used to analyze apoptotic cells in the cells. For PDT experiments, a fully automatic optical

power meter (CEL-NP2000-2(10)A) and a multi-functional fiber optic light source module set (CEL-FES300CEL-LB70) from Beijing China EDUCATION Au-Light Technology Co., Ltd. were used. The experimental mice were imaged using an IVIS® Lumina XR series III system (PerkinElmer, USA) for *in vivo* fluorescence imaging.

2.3 Synthesis of compound I-BODIPY 4 (B4)

Compound **B3** (200 mg, 0.32 mmol) and anisic aldehyde (173.2 mg, 1.27 mmol) were dissolved in toluene (29 mL) and added with acetic acid (glacial, 0.6 mL, 11.52 mmol) and pyridine (0.9 mL, 7.8 mmol). The resulting mixture was refluxed for several h. The solvent was then concentrated under reduced pressure and the residue was diluted with ultrapure water (20 mL) and extracted with DCM. The extract was dried with anhydrous sodium sulfate and the solvent was evaporated. The resulting material was purified by silica gel column chromatography (DCM/hexane = 1/1, v/v) to yield green solid **B4** (60% yield). ^{1}H NMR (400 MHz, CDCl$_3$): δ 8.13 (d, J = 16.6 Hz, 2H), 7.71–7.52 (m, 6H), 7.20 (d, J = 8.7 Hz, 2H), 7.12 (d, J = 8.7 Hz, 2H), 6.95 (d, J = 8.8 Hz, 2H), 4.79 (s, 2H), 3.86 (s, 6H), 2.58 (t, J = 2.4 Hz, 1H), 1.49 (s, 6H); HRMS m/z: C$_{38}$H$_{31}$BF$_2$I$_2$N$_2$O$_3$ [M + Na]$^+$ calcd for 889.0383 found 889.0334.

2.4 Preparation of CIB NPs

The fabrication of CIB NPs was achieved *via* a self-assembly approach. Briefly, solutions of CAT and **B4** were coalesced in various ratios for self-assembly. Initially, highly concentrated stock solutions were prepared. Precisely, 1 mg of CAT was accurately weighed and dissolved in 1 mL of PBS (pH = 7.4) solution to create a concentrated CAT stock solution, and 1 mg of **B4** was likewise dissolved in 1 mL of DMSO, forming a high-concentration **B4** stock solution. Subsequently, these stock solutions were subjected to dilution. Namely, 0.275 mL of the concentrated CAT solution was combined with 0.725 mL of PBS solution to create a diluted CAT solution, and similarly, 0.009 mL of the concentrated **B4** solution was mixed with 0.991 mL of DMSO to formulate a diluted **B4** solution. Following this, the diluted CAT and **B4** solutions were amalgamated in differing proportions. Four distinct ratios, namely CAT : **B4** = (5 : 1), (1 : 1), (1 : 5), and (1 : 10), were utilized in this study. The amalgamated solution was sonicated for 30 min at 0 °C within an ultrasonic cleaner under dark conditions. Thereafter, magnetic stir bars were introduced into the assembly solution, and the diverse ratio assembly solutions were stirred gently on a magnetic stirrer at ambient temperature for 2 h. The resulting four types of assembled nanoparticles with various ratios were preserved at 4 °C in the dark until further use. A similar method was employed to fabricate BSA-I-BODIPY NPs (BIB NPs) *via* the self-assembly of Bovine Serum Albumin (BSA) and **B4**.

2.5 Study on assembly dynamics of CIB NPs

CIB NPs, assembled in a molar ratio of CAT : **B4** = 1 : 1, were subjected to ultrasonication and then slowly stirred on a magnetic stirrer for varying durations. The NPs were subsequently

slowly added into 2 mL of PBS (pH 7.4) and mixed thoroughly by sonication before measurement of particle size using a DLS instrument in a designated vessel.

2.6 Stability of CIB NPs

1 mL of CIB NPs solution was mixed with 2 mL of PBS (pH 7.4) and sonicated. The resulting mixture was then added to a designated measurement cell for DLS analysis. The particle size of CIB NPs at different time points was monitored for 72 h.

2.7 Determination of oxygen production and consumption

The oxygen generation of CIB NPs in H_2O_2 solutions of different concentrations was determined. First, 10 μL, 25 μL, 50 μL, and 100 μL of H_2O_2 stock solution (approximately 10 mM) were dissolved in 10 mL of ultrapure water to obtain 10 μM, 25 μM, 50 μM, and 100 μM H_2O_2 solutions, respectively. CIB NPs (10 μM) were added to each solution, and the oxygen generation of H_2O_2 was immediately measured using a portable dissolved oxygen meter from 0 s to 120 s.

The oxygen generation of CIB NPs in solutions of different pH values was determined. Different pH solutions were prepared according to the buffer solution preparation method, with solution pH values of 5.7, 6.0, 6.5, 7.0, and 7.5. Next, CIB NPs were added to 50 mL of pH = 5.7 water solution, followed by the addition of 100 μL of H_2O_2 solution. The oxygen generated from 0 s to 120 s was immediately measured using a portable dissolved oxygen meter, and the data were recorded. The same method was used to measure the oxygen generation in water solutions of other pH values.

The oxygen generation of CIB NPs after photodepletion of oxygen was determined. First, the H_2O_2 solution was prepared using the same method. Next, CIB NPs were added to the H_2O_2 solution and left in the dark for 10 min, followed by measuring the oxygen generation from 0 s to 120 s using a measuring instrument. Then, CIB NPs were added to the H_2O_2 solution and exposed to 650 nm light for 10 min, followed by measuring the oxygen generation from 0 s to 120 s using a dissolved oxygen meter. Finally, the oxygen generation of H_2O_2 solution without CIB NPs and exposure to light was measured from 0 s to 120 s.

The oxygen consumption of CIB NPs after light exposure was determined. First, the H_2O_2 solution was prepared using the method described above. Next, CIB NPs were added to the H_2O_2 solution and the oxygen generation from 0 s to 120 s was immediately measured using a dissolved oxygen meter. Subsequently, the H_2O_2 solution was exposed to 650 nm red light for 30 min, and the oxygen consumption data were recorded using a measuring instrument at 5 min intervals.

2.8 Cellular dark toxicity study

Preparation of A549 cell suspension and cell counting were performed. A549 cells were seeded in a 96-well plate at a density of 5000 cells per well in 100 μL of F-12K medium. The plate was then incubated overnight in a dedicated incubator to allow cell adhesion and growth. The Cell counting kit-8 (CCK-8) method was used to set up the blank group, control group, and experimental group, where CIB NPs were added to the medium at the concentrations specified in the experimental design. Each group consisted of five wells to ensure reliable results. The blank group contained only a complete medium without A549 cells or CIB NPs, while the control group contained A549 cells and a complete medium without CIB NPs. The experimental group contained A549 cells, a complete medium, and different concentrations of CIB NPs. After the specified exposure time, the CIB NPs solution was removed, and the cells were washed three times with PBS. Then, 100 μL of CCK-8 solution was added to each well, and the plate was incubated for approximately 1 h until the CCK-8 dye was completely converted and a visible colour change was observed. If the colour change was not apparent, the reaction time was prolonged. The absorbance values at 450 nm were measured to determine the metabolic activity and relative cell number. By comparing the absorbance values of the experimental and blank control groups, the toxicity of CIB NPs to A549 cells was evaluated, and a range of drug concentrations that were relatively safe could be screened.

2.9 *In vitro* cellular uptake experiments and optimal enrichment time

A total of 10^5 A549 cells were seeded in laser confocal glass bottom culture dishes and incubated in a dedicated incubator containing F-12K complete culture medium. After 18 h of incubation, 1 mL of flash medium containing CAT-I-BODIPY NPs (10 μM) was injected into the cells and then incubated for 1 h, 3 h, 6 h, and 12 h, respectively. After incubation, the cells were washed three times with 1× PBS buffer and then F-12K basal medium was added. Confocal laser scanning microscopy (CLSM) was used to observe the cells with an excitation wavelength of 650 nm.

2.10 Intracellular production of singlet oxygen experiment

The experiment was designed with four groups: control group, control + laser group, BSA-I-BODIPY NPs + laser group, and CAT-I-BODIPY NPs + laser group. The procedure was as follows: A549 cells were seeded in several confocal glass-bottom culture dishes, and the probes were added after the cells adhered to the wall. Subsequently, the cells were illuminated with light (650 nm, 300 mW cm^{-2}) for 15 min, washed with PBS three times, and then incubated with F-12K basal medium containing Singlet Oxygen Sensor Green (SOSG) for 10 min. After washing with PBS three times, 1 mL of F-12K basal medium was added, and the stained cells were imaged using a 60x magnification CLSM.

2.11 Cellular phototoxicity studies

The experimental procedure for phototoxicity was similar to that of dark toxicity. A549 cells were co-cultured with CIB NPs for a certain period (8 h), followed by 15 min of 650 nm light exposure (300 mW cm^{-2}). The viability of the cells was evaluated afterwards.

2.12 *In vitro* therapeutic effect

To directly demonstrate the effective phototoxicity of CIB NPs on A549 cells, calcein acetoxymethyl ester (Calcein-AM)/propidium iodide (PI) was used for dual-colour fluorescence staining of live/dead cells to identify living and dead cells. Two experimental groups were designed in this study. The first group included experimental groups with different light powers (0 mW cm^{-2}, 100 mW cm^{-2}, 200 mW cm^{-2}, 300 mW cm^{-2} and 400 mW cm^{-2}) under fixed light exposure time (15 min). A549 cells were incubated with Calcein-AM/PI solution at room temperature for 15 min. Subsequently, dual-stained cell images were obtained using a CLSM under a 20× objective lens. The second group included a control group without light exposure, a control + laser group with light exposure, a BIB NPs + laser group with light exposure, and a CIB NPs + laser group with light exposure. The cell operation procedure was the same as before. A549 cells were incubated with Calcein-AM/PI solution at room temperature for 15 min. Subsequently, dual-stained cell images were obtained using a CLSM under a 20× objective lens.

2.13 Flow cytometry

In the experiment, A549 cells were cultured in four groups of culture media, including the control group, control + laser group, BIB NPs + laser group, and CIB NPs + laser group. During the culture process, the cell density and treatment time of each group should be kept consistent, and cell growth should be ensured. Next, we collected the cells from the culture bottle into a centrifuge tube using digestion enzymes such as trypsin and washed the cells with sterile PBS or cell culture medium. Then, we suspended the cells in 1× binding buffer, gently shaking them to make the cells evenly suspended, to prepare the cell suspension for subsequent flow cytometry analysis. To detect the apoptosis rate of the cells, we used a cell apoptosis detection kit for staining, which includes staining agents such as Annexin V-FITC and PI. Finally, we used flow cytometry to detect the scatter and fluorescence signals in the cell suspension and used FlowJo software for data processing and statistical analysis.

2.14 *In vivo* fluorescence imaging

When the tumour volume reached approximately 50 mm^3, 200 μL of a solution containing CIB NPs (200 μM) was injected. Small animal imaging was performed at different time points after injection to monitor the fluorescence signal distribution of CIB NPs in the body and determine the optimal light exposure time window for PDT.

2.15 Evaluation of *in vivo* PDT efficacy in subcutaneous tumours

To validate the photodynamic therapeutic effect of CIB NPs *in vivo*, the present study divided nude mice into four groups: group 1 (control) received an injection of PBS; group 2 (control + laser) received an injection of PBS and was exposed to 650 nm light for a total of 15 min in the tumour region; group

3 (BIB NPs + laser) received an injection of BIB NPs followed by exposure to 650 nm light for a total of 15 min in the tumour region, and group 4 (CIB NPs + laser) received an injection of CIB NPs followed by exposure to 650 nm red light for a total of 15 min in the tumour region. Each group consisted of 3 nude mice, which were intravenously injected with PBS (200 μL), PBS (200 μL), BIB NPs (200 μL, 200 μM), and CIB NPs (200 μL, 200 μM), respectively. 18 h after injection, the tumour region was exposed to 650 nm light at a power density of 300 mW cm^{-2} for 15 min. Tumour volume was measured using a caliper in all nude mice for the following 2 weeks, and tumour volume was calculated based on the long and short diameters. On day 15, the mice were euthanized, and the tumour tissue was carefully dissected using ophthalmic scissors and forceps. The left and right kidneys, spleen, right upper abdomen liver, lungs, and heart were then exposed and removed sequentially. Tumour short and long diameters and weights were recorded. The obtained tumour tissue was stained with hematoxylin and eosin (H&E) and TUNEL.

2.16 *In vivo* biosafety evaluation

To evaluate the *in vivo* biosafety of CIB NPs, we regularly weighed the mice and performed H&E staining on the major organs obtained after dissection for histological analysis.

2.17 Animal ethics statement

All animal procedures were performed in accordance with the Guidelines for Care and Use of Laboratory Animals of Hainan Medical University and approved by the Animal Ethics Committee of Hainan Medical University.

2.18 Statistical analysis

Data were analyzed using SPSS 22.0 software. All statistical data are presented as mean ± standard deviation (mean ± S.D.). Differences between multiple groups were analyzed by one-way analysis of variance (ANOVA). Differences were considered statistically significant when $p < 0.05$.

3. Results and discussion

3.1 Synthesis and characterization of B1–B4

To synthesize the I-BODIPY candidate (**B4**), we employed a four-step process involving a condensation reaction, two substitution reactions, and a Knoevenagel condensation reaction (Fig. 1a). Each of **B1**, **B2**, **B3**, and **B4**, when dissolved in DCM, presented distinct and vibrant colours under sunlight and UV light (Fig. S2†). The structures of **B1**, **B2**, **B3**, and **B4** were confirmed through ^{1}H NMR and mass spectrometry analyses (Fig. S3–S10†). After successful synthesis, we investigated the optical properties of these compounds. **B1** and **B2** showed similar absorption and fluorescence emission spectra, with $\lambda_{\max,\ \text{Abs}}$ and $\lambda_{\max,\ \text{Em}}$ both located at 500 nm and 545 nm, respectively (Fig. S11 and S12†). These similar spectra could be due to the unaltered position of the BODIPY core. **B3** displayed a red-shifted emission peak and a roughly four-fold decrease

a)
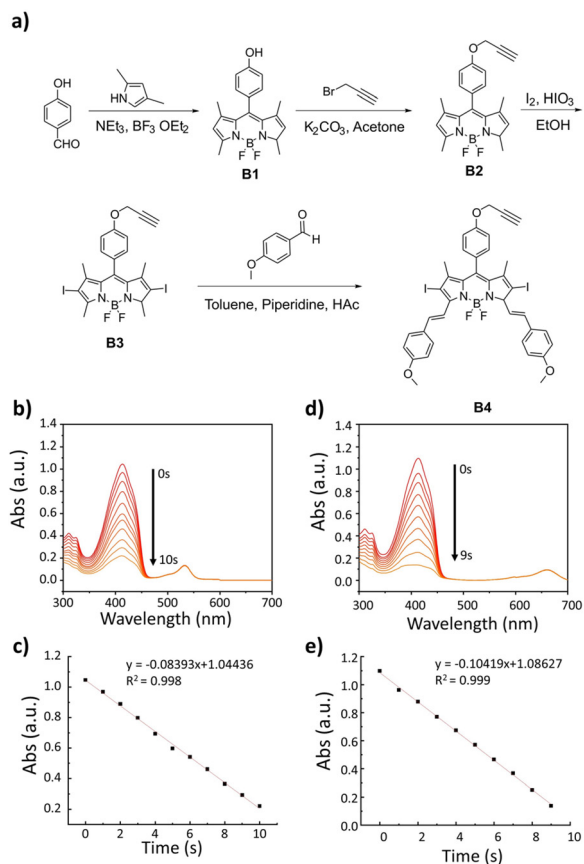
Fig. 1 (a) Synthetic routine for I-BODIPY. (b) The absorbance degradation of DPBF in the appearance of **B3** as PSs under irradiation of Xe lamp. (c) Linear fitting of absorbance degradation in (b). (d) The absorbance degradation of DPBF in the appearance of **B4** as PSs under irradiation of Xe lamp. (e) Linear fitting of absorbance degradation in (d).

in fluorescence intensity compared to **B2** (Fig. S14†), possibly due to the incorporation of heavy atoms (iodine) at positions 2 and 6 of the BODIPY core. This modification may also boost the spin–orbit coupling effect in the molecule, thus enhancing the intersystem crossing rate and increasing the production of singlet oxygen ($^1O_2$) quantum yield (Φ_Δ) by PSs. The addition of an electron-donating 4-methoxyphenyl substituent to the BODIPY core (**B4**) resulted in a redshift in the absorption and fluorescence emission spectra (Fig. S15 and S17†). The calculated Φ_Δ was 73% and 67%, respectively according to the established methodology,[41] indicating excellent PDT efficacy (Fig. 1b–e, Fig. S1†). Moreover, the redshift of **B4** to the NIR region could effectively overcome the issue of tissue penetration depth, making it an ideal candidate for imaging-guided PDT.

3.2 Assembly of CIB NPs

To achieve efficient PDT targeted at the hypoxic tumour microenvironment while maintaining high biocompatibility, we introduced the protein CAT into the system to provide an *in situ* oxygen supply. Guided by hydrophobic and hydrophilic interactions between **B4** and CAT, and hydrogen bonding within the CAT protein itself, these functional units self-

assembled in an orderly fashion due to multiple supramolecular interactions. The resulting water-soluble and biocompatible CAT-I-BODIPY NPs were optimized under specific assembly conditions, and fluorescent nanoprobes were designed and built under varying assembly conditions. These NPs were then characterized using TEM, DLS, and fluorescence spectroscopy. In the assembly system, when the CAT concentration was high (CAT : **B4** = 5 : 1), we observed that the particle size of NPs was very small (Fig. S20 and S21†), which suggested that the number of **B4** molecules was insufficient to drive effective assembly at this concentration of CAT. Conversely, when the concentration of **B4** molecules was high (CAT : **B4** = 1 : 5), we observed larger nanoparticle aggregates in TEM (Fig. S22†). This could be due to the hydrophobic aggregation of excess **B4** molecules through π–π interactions, resulting in the formation of larger aggregates. Interestingly, when CAT and **B4** were adjusted to a 1 : 1 concentration ratio, spherical NPs with uniform size and an average diameter of about 100 nm were observed by TEM, and were named CAT-I-BODIPY NPs (Fig. 2a). At this ratio, the hydrophobic nature of BODIPY molecules led them to congregate near the hydrophobic region of CAT, thus enabling the assembly of CAT into an ordered nanostructure governed by hydrophilic and hydrophobic interactions and protein–protein hydrogen bonding. This self-assembled nanomaterial could effectively integrate multiple CAT and **B4** molecules in an organized manner, therefore optimizing the function of each unit, such as FI, PDT, and CAT's *in situ* oxygen generation ability, achieving enhanced PDT with FI-guided *in situ* oxygen supply. The hydrodynamic diameter and polydispersity index of CAT-I-BODIPY NPs were found to be 118.2 nm and 0.171, respectively, indicating a high level of monodispersity and uniformity (Fig. 2a, inset). Interestingly, compared to the other three groups, the peak fluorescence intensity of CIB NPs in the fluorescence spectrum was the highest, demonstrating that the ordered assembly could preserve the functionality of the assembly units themselves (Fig. 2b). Through the characterization of different assembly conditions using TEM, DLS, and fluorescence spectroscopy, we discovered that the optimal condition was when the CAT concentration was approximately equal to the **B4** concentration (CAT : **B4** = 1 : 1).

3.3 Analysis of assembly kinetics, stability of CIB NPs and loading capacity of B4

Further assembly kinetics studies were conducted on CIB NPs under this optimal assembly condition. As shown in Fig. 2c, the hydrodynamic diameter increased gradually as the assembly proceeded, which was almost completed in 2 h with a final size of about 120 nm. Notably, it was found that the assembled CIB NPs could remain stable with uniform size in aqueous solution for up to 72 h (Fig. 2d). Besides, we have also assessed the size change of the assembly under different pH conditions including simulated physiological and pathological conditions. The results show that the nanoassemblies can maintain stable particle sizes under various conditions, thus avoiding the release of **B4** candidates (Fig. S27†). In addition to size stability, we also investigated the optical properties of the
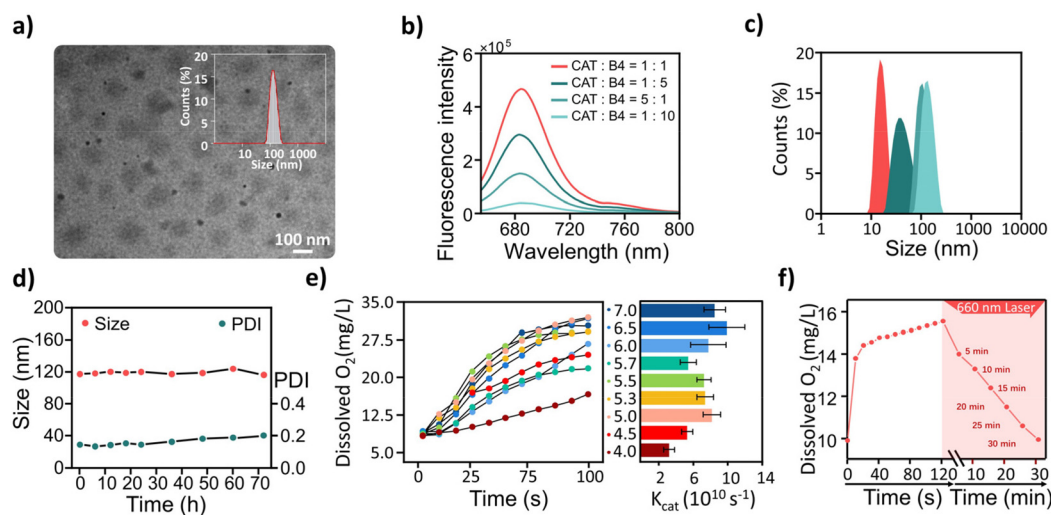
Fig. 2 Characterization of CIB NPs. (a) Transmission electron microscopy (TEM) image of CIB NPs at an equal concentration of CAT and **B4** (CAT : **B4** = 1 : 1) with a scale bar of 100 nm. The inset showed the dynamic light scattering (DLS) measurement of the CIB NPs at an equal concentration of CAT and **B4** (CAT : **B4** = 1 : 1). (b) Fluorescence spectra of CAT and **B4** under different assembly conditions. (c) Assembly kinetics of CIB NPs. (d) Particle size and polydispersity index (PDI) of CIB NPs measured by DLS over 72 h. (e) Oxygen generation and catalytic efficiency of CIB NPs at different pH conditions and relative catalytic activity. (f) The dissolved oxygen content of CIB NPs after light irradiation.

nanoassemblies under different pH conditions. The FL spectra results further confirm that the nanoassemblies remain stable and retain excellent fluorescent properties and singlet oxygen generation ability across the physiological and pathological pH range (Fig. S28 and S29†). Zeta potential analysis also demonstrated that the CIB NPs maintained a relatively consistent zeta potential over 72 h, indicating their good stability (Fig. S30†).

To estimate the loading capacity of our nanoparticles, we first considered the dimensions of the protein assembly and the dimensions of the nanoparticles. The protein assembly,
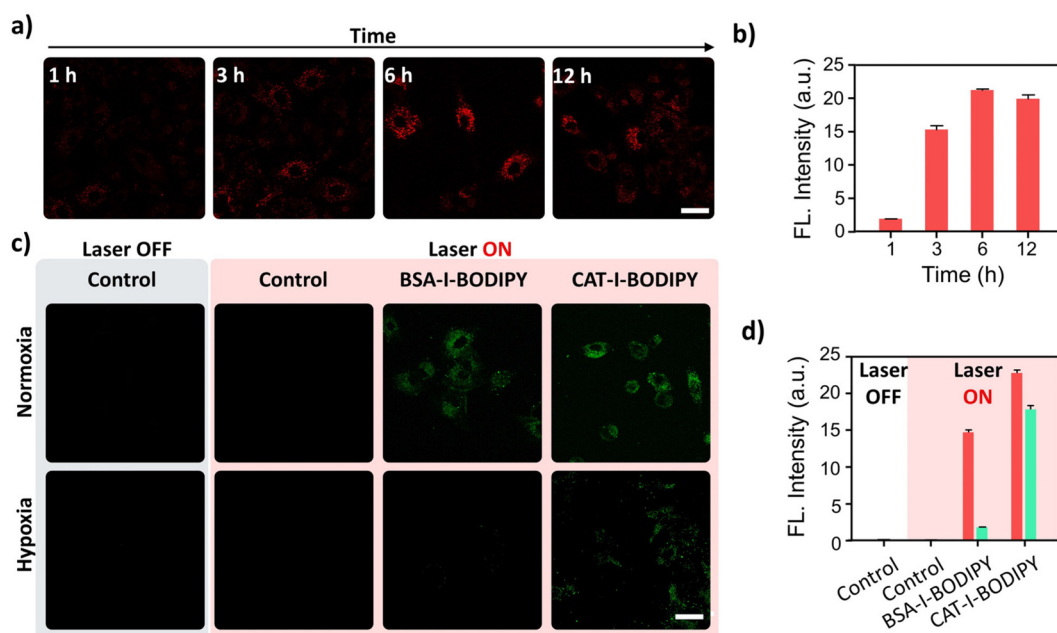
Fig. 3 (a) CLSM images of A549 cells were obtained after incubation with CIB NPs for different periods. (b) The relative fluorescence intensity of A549 cells in (a) was measured after incubation with CIB NPs at different times. (c) CLSM images of A549 cells were obtained after staining with SOSG following treatment with CIB NPs both in normoxic and hypoxic conditions, with or without 650 nm laser illumination. (d) The relative fluorescence intensity of A549 cells in (c) was measured after staining with SOSG following treatment with CIB NPs, with or without 650 nm laser illumination. Scale bar: 40 μm.

based on PDB code 7P8 W, was found to have dimensions of approximately 9.83 nm, implying a radius of about 4.915 nm. Thus, the volume of the protein assembly can be approximated as $V_{protein} = 4/3 \times \pi \times (4.915 \text{ nm})^3 = 248.87 \text{ nm}^3$. The nanoparticle size was measured to be approximately 118.2 nm in diameter in DLS, suggesting a radius of about 59.1 nm. Therefore, the volume of the nanoparticle can be approximated as $V_{nano} = 4/3 \times \pi \times (59.1 \text{ nm})^3 = 868758.065 \text{ nm}^3$. Based on these volumes, we estimated the number of proteins that could fit into a single nanoparticle as num_proteins = $V_{nano}/V_{protein}$ = 868758.065 nm^3/248.87 nm^3 = approximately 3490 proteins. On the other hand, our computational model, which is primarily based on docking simulations, provides valuable predictions on the interaction between these two entities. In Fig. S25 and S26,† we've displayed the docking of the entire complex and a zoomed-in view of the interaction area, respectively. We found that several residues (382ARG, 383VAL, 385ASN, 63HIS, 387GLN, 388ARG, 389ASP, 398GLN, 397ASN, 396ASP, 395GLN, 394MET, 369ASN, 372HIS, 374PRO, 377CYS, 395GLN, 394MET) are interacting with the small molecule. As for the loading capacity, based on our computations and the dimensions of the protein and the nanoparticle, we estimate that each nanoparticle could potentially accommodate around 3489 tetrameric protein complexes. Given that our model suggests each protein tetramer binds one **B4** molecule, this would suggest the maximum loading capacity of approximately 3489 **B4** molecules per nanoparticle.

Regarding the loading rate, we have analyzed the assembly kinetics data using a first-order kinetic model. The nanoparticle sizes at different time points (10, 30, 60, and 120 min) were measured to be 14.91 nm, 39.58 nm, 105.1 nm, and 134.16 nm, respectively. From this data, the rate constant k was estimated to be 0.0189 min^{-1}, suggesting a significant assembly activity over time.

3.4 Determination of oxygen production and consumption

Since CAT can effectively catalyze the decomposition of H_2O_2 into oxygen in the acidic microenvironment of tumours, it is essential to evaluate its catalytic activity after assembly. Compared with free CAT, it was found that the designed self-assembled nanoplatform had higher oxygen production under the same conditions (Fig. S32†). We hypothesize that the con-
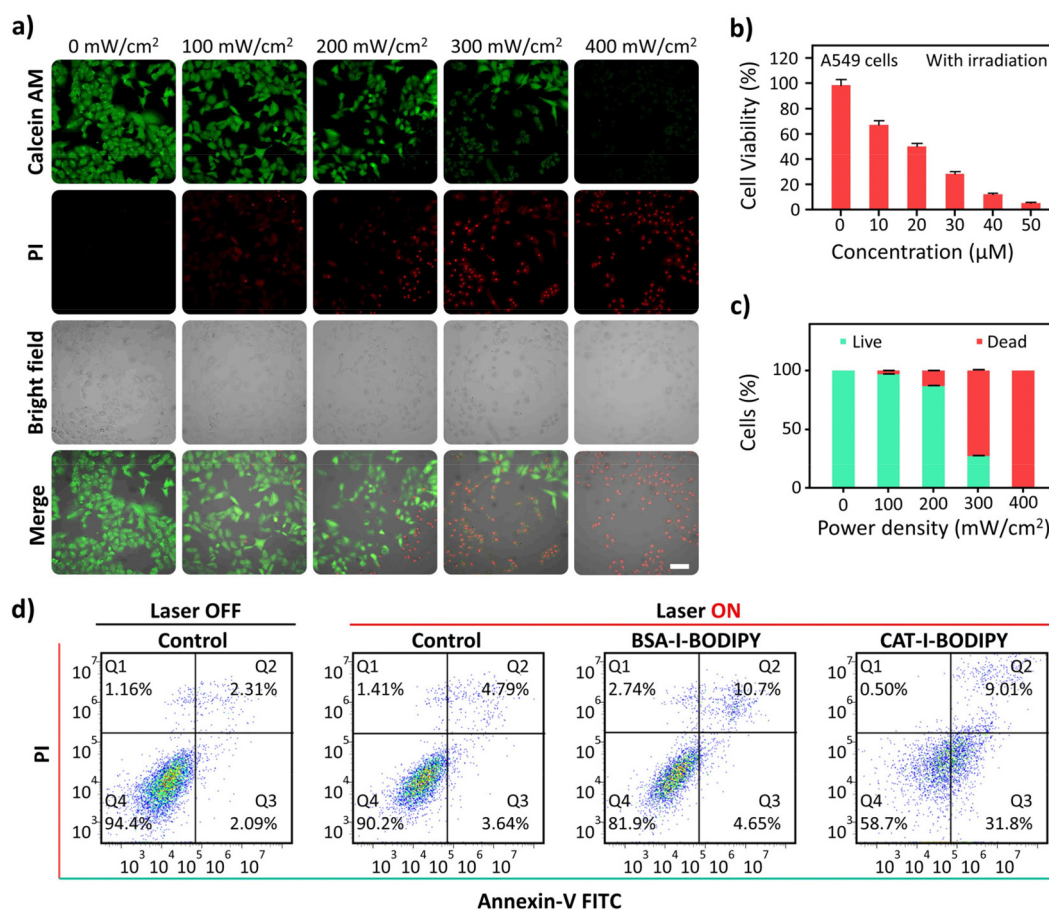
Fig. 4 (a) CLSM images of A549 cells treated with different light powers and stained with Calcein-AM and PI. Scale bar: 100 μm. (b) The effect of different concentrations of CIB NPs on A549 cell viability after 15 min of 650 nm light irradiation (300 mW cm⁻²) was tested by a CCK-8 assay. (c) The relative fluorescence intensity of A549 cells in (a) stained with Calcein-AM and PI after different treatments. (d) Flow cytometry assay of different treatments.

fined space within the assembled structure allows for a faster catalytic reaction of the substrate, thereby effectively improving the catalytic efficiency of CAT. It was found that even at low H_2O_2 concentrations, CIB NPs maintained their catalytic activity in decomposing H_2O_2 to produce O_2, and the amount of oxygen produced increased with the increase of H_2O_2 concentration (Fig. S31†). As shown in Fig. 2e, the CIB NPs could maintain superb catalytic efficiency in acidic conditions, confirming the availability in tumour microenvironments. To further investigate the pH effect on catalytic ability, we performed additional enzyme activity assays. The results revealed that the catalytic activity of the assembled CIB NPs is enhanced under slightly acidic conditions. We calculated the k_{cat} values by dividing the maximum rate of the reaction (V_{max}) by the total enzyme concentration. These values, under the condition of substrate saturation, provide a measure of the intrinsic catalytic power of the enzyme (Fig. 2e, right). The concentration of dissolved oxygen in CIB NPs under varying illumination times was also investigated (Fig. 2f). The results indicated a significant decrease in dissolved oxygen concentration under light irradiation, confirming I-BODIPY-induced PDT as an oxygen-consuming process and suggesting that laser illumination for 15 min should be suitable due to the maintenance of O_2 capacity with the existence of CAT.

3.5 Biocompatibility and cellular uptake of CIB NPs

In vitro cytotoxicity analysis was performed under dark conditions on A549 and 4T1 cells using the CCK-8 assay. The results revealed that cell viability was not significantly affected by CIB NPs at various concentrations (Fig. S33 and S34†), which confirmed the biocompatibility of CIB NPs, suggesting their potential applicability for different tumour cells. The cellular uptake and imaging capability of CIB NPs were evaluated by co-culturing them with A549 cells at 37 °C and examining the cells using CLSM. A bright red fluorescence was emitted by CIB NPs, which were located in the cytoplasm of A549 cells under 650 nm laser excitation, indicating their potential for visualization (Fig. 3a). Changes in cellular fluorescence at different incubation times showed that the brightness of the cells gradually increased, reaching its maximum at 6 h, which suggests optimal enrichment of CIB NPs in tumour cells (Fig. 3a and b).

3.6 $^1O_2$ generation ability of CIB NPs in cells

Reactive oxygen species (ROS), especially singlet oxygen, serve as the primary cytotoxic agent in photodynamic therapy (PDT), being generated by photosensitizers (PSs) upon light activation and leading to the destruction of tumour cells. Singlet Oxygen Sensor Green (SOSG), a specific fluorescent probe, effectively visualizes $^1O_2$ production by emitting intense green fluorescence upon reaction. In our study, we observed that, in the absence of our nanoprobe (control and control + laser groups), $^1O_2$ generation was negligible.

However, with the introduction of our BIB NPs + laser, we witnessed pronounced green fluorescence, indicative of significant $^1O_2$ generation attributable to the **B4** molecules within
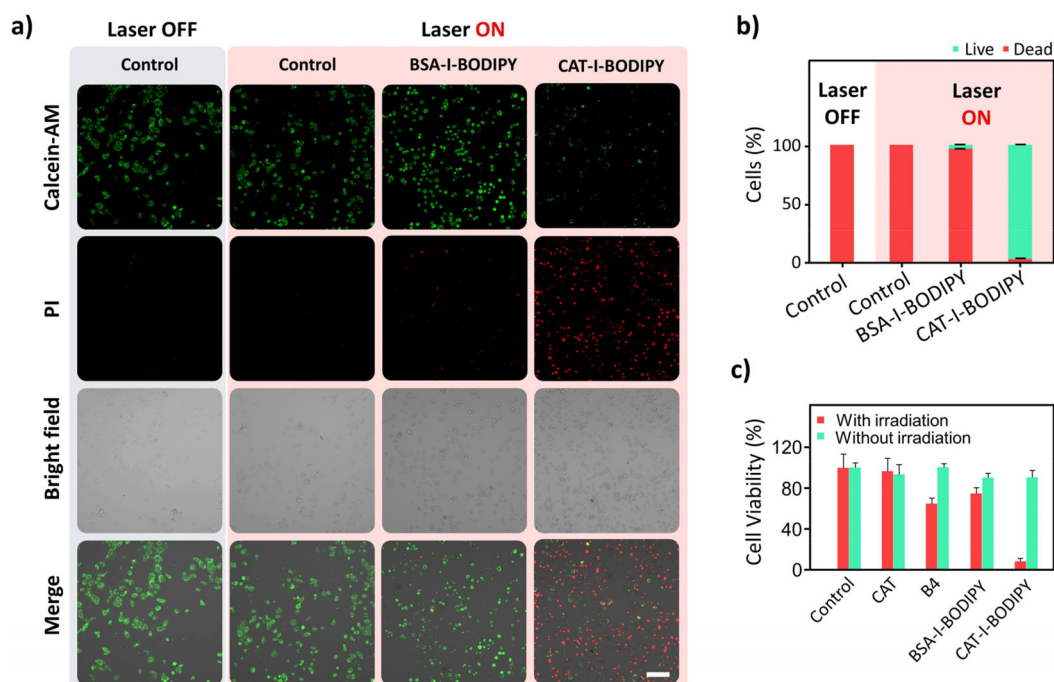
Fig. 5 (a) CLSM images of A549 cells stained with Calcein-AM and PI after conducting different treatments were displayed in hypoxic conditions. Scale bar: 100 μm. (b) The relative fluorescence intensity of A549 cells in (a) stained with Calcein-AM and PI after different treatments. (c) The effect of different groups (control, CAT, **B4**, BSA-I-BODIPY NPs, CAT-I-BODIPY NPS on A549 cell viability under hypoxic conditions after 15 min of 650 nm light irradiation (300 mW cm^{-2}) was tested by a CCK-8 assay.

our probe. Remarkably, the fluorescence intensity increased substantially in the CIB NPs + laser group (Fig. 3c, normoxia). This enhanced effect stems from the oxygen produced by the catalase (CAT) integrated into our nanoplatform, boosting the PDT effect of **B4** molecules and leading to a higher yield of $^1O_2$. Significantly, even under hypoxic conditions, a significantly brighter green fluorescence could be observed in the CAT-I-BODIPY NPs (Fig. 3c and d, hypoxia). This confirms the potency of our CIB NPs as effective PSs for PDT, simultaneously augmenting the treatment's impact on hypoxic tumours and enabling real-time guidance *via* fluorescence imaging.

3.7   *In vitro* therapeutic effect

To study the *in vitro* therapeutic effect, A549 cells containing CIB NPs were exposed to different light powers for 15 min. The results showed that as the light power increased, the green fluorescent cells stained with Calcein-AM gradually decreased, while the red fluorescent cells stained with PI gradually increased, and when 300 mW cm^{-2} was reached, a large number of red fluorescent cells and a small amount of green fluorescent cells were observed, indicating that

300 mW cm^{-2} can be served as proper laser power density (Fig. 4a and c).

In vitro cell phototoxicity analysis using the CCK-8 assay on A549 and 4T1 cells revealed that cell viability decreased with increasing doses of CIB NPs under light irradiation (Fig. 4b and Fig. S35†). At concentrations between 30 μM to 50 μM, most cells were nonviable. CIB NPs showed a decent inhibitory effect on both cell types after incubation for 15 min of 650 nm NIR light irradiation at 300 mW cm^{-2}, suggesting the strong potential of CIB NPs as PDT candidates with antitumor effects on different tumour cells. Preliminary experimental results indicated that the combination of CIB NPs and light irradiation generated a large amount of $^1O_2$, enhancing the therapeutic effect of PDT. Morphological changes of cells under different conditions were observed using Calcein-AM/PI dual staining (green: live cells; red: dead cells). Results showed that the CIB NPs + laser group exhibited strong red fluorescence and lost cell shape, indicating that CIB NPs effectively killed A549 cells (Fig. S36 and S37†).

Annexin V-FITC/PI double staining assay was used to investigate the apoptotic effect of the designed NPs. The apoptotic rate was negligible in control and control + laser groups but
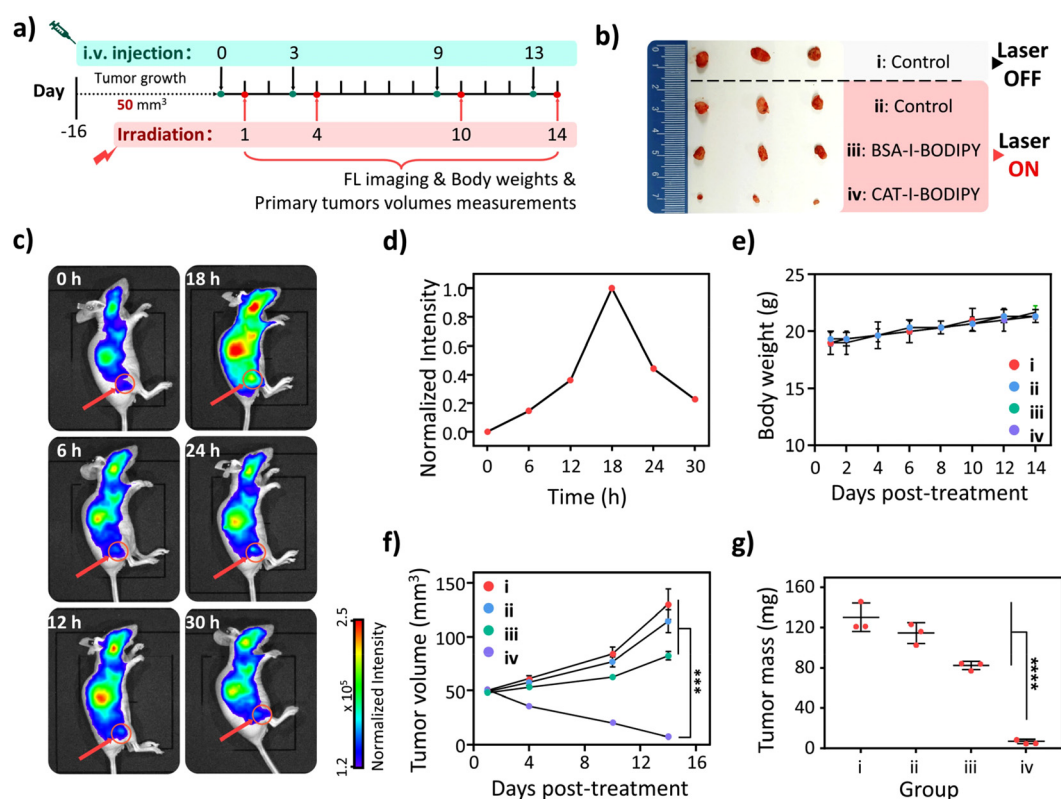
Fig. 6   *In vivo* application of CIB NPs. (a) Schematic diagram of the xenograft A549 tumour-bearing nude mouse model construction and *in vivo* NIR imaging-guided enhanced PDT plan in mice. (b) Images of tumours collected from different groups of nude mice 15 days after treatment. (c) Real-time fluorescence imaging was performed on A549 tumour-bearing nude mice after intravenous injection of CIB NPs. (d) The relative fluorescence intensity of *in vivo* fluorescence imaging in (c) was measured on A549 tumour-bearing nude mice after intravenous injection of CIB NPs. (e) The body weight of nude mice was measured after different treatments. (f) Tumor volume in nude mice was compared after various treatments. Data were presented as mean ± SD, ***p < 0.001. (g) The tumour mass of nude mice after different treatments is presented in mean ± SD (standard deviation), with statistical significance indicated as ****p < 0.0001.

increased after treatment with BIB NPs (15.35%) (Fig. 4d). In comparison, the apoptotic rate of CIB NPs was the highest (40.81%), indicating that CIB NPs induced apoptosis in A549 cells. To investigate the feasibility of using CIB NPs for *in vivo* tumour treatment, experiments were conducted on nude mice with solid tumour models established by injecting A549 cells subcutaneously.

To evaluate the PDT effect under hypoxic conditions, the CAT-I-BODIPY NPs exhibited intense red fluorescence, indicating a high proportion of cell death (Fig. 5a and b). Compared to the group without CAT, the CAT-I-BODIPY NPs group led to an increased generation of singlet oxygen and cell-killing capability, demonstrating the enhanced PDT effect in the designed CAT-I-BODIPY NPs. Notably, we performed cell viability assays using CCK-8, as well as hypoxic phototoxicity experiments under hypoxic conditions (Fig. 5c). Under non-irradiation conditions, we found that all groups demonstrated high cell viability, indicating the safety of our materials. However, under laser illumination, the control and CAT groups continued to exhibit high cell survival rates. While the **B4** and BIB groups showed some cytotoxic effects, which may be restricted by hypoxia that affected its phototherapeutic efficacy. Interestingly, the CIB group displayed a significant rate of cell apoptosis under these conditions, which implied a strong cell-killing effect. The results from our cell viability and hypoxic phototoxicity experiments provided further support for these observations, thereby substantiating the effectiveness of our CIB NPs in promoting cell apoptosis under hypoxic conditions.

3.8 Evaluation of *in vivo* imaging-guided PDT efficacy in subcutaneous tumours

In vivo fluorescence intensity was measured at different time points, showing that CIB NPs easily penetrated tumour tissue through nutrient blood vessels. Fig. 6c demonstrated that following intravenous injection, fluorescence intensity at the tumour site gradually increased, peaking at 18 h post-injection. The liver displayed the brightest fluorescence intensity due to the metabolic accumulation of CIB NPs, which decreased significantly after 24 h, indicating rapid metabolic degradation *in vivo*. Consequently, PDT was performed at the 18 h time point (Fig. 6d). *Ex vivo* fluorescence imaging on A549 tumour-bearing nude mice 30 h after the intravenous injection of CIB NPs also observed a minor fluorescence in the liver and tumour regions, while other major organs showed negligible fluorescence (Fig. S39†). To evaluate CIB NPs' efficacy in PDT on nude mouse tumours, surface blood was washed from tumours, and morphological and size changes were observed visually. Fig. 6b revealed that tumour growth was evident in the control group with and without irradiation, while it decreased slightly in the BSA-I-BODIPY + laser group and significantly in the CIB NPs + laser group. Tumor volume changes for each group were shown in Fig. 6f. After multiple PDT treatments for 15 days, tumour volumes in the control groups increased rapidly, while the BIB NPs + laser group experienced a slower increase and the CIB NPs + laser group

exhibited a significant decrease. Tumour mass for each group was presented in Fig. 6g, showing a significant reduction in the CIB NPs + laser group. These results indicated that *in situ* oxygen production by CAT in the CIB NPs + laser group significantly enhanced $^1O_2$ generation, inhibiting tumour growth and reducing tumour size. In contrast, the BIB NPs + laser group displayed weaker anti-tumour effects due to the hypoxic environment. The control groups' rapid tumour proliferation eliminated the influence of NIR radiation on tumour inhibition.

Therapeutic effects were microscopically evaluated by sampling nude mouse tumours from each group and conducting H&E staining histological analysis (Fig. 7). The CIB NPs + laser group exhibited a vast number of dead tumour cells, indicating a significant enhancement in tumour cell killing *via* CIB NPs-mediated PDT. H&E staining of tumour tissue indicated that the CAT-I-BODIPY group exhibited more pronounced morphological alterations and extensive necrosis, suggesting effective therapy. In contrast, the BSA-I-BODIPY group showed a lower cancer cell density but lacked significant morphological changes or necrosis. In addition to the H&E staining, we also performed a TUNEL assay to assess the apoptosis rate in tumour tissues following treatments. The TUNEL assay results also revealed a significantly higher apoptosis rate in the CAT-I-BODIPY group compared to the BSA-I-BODIPY group, further affirming the superior therapeutic efficacy of CAT-I-BODIPY.
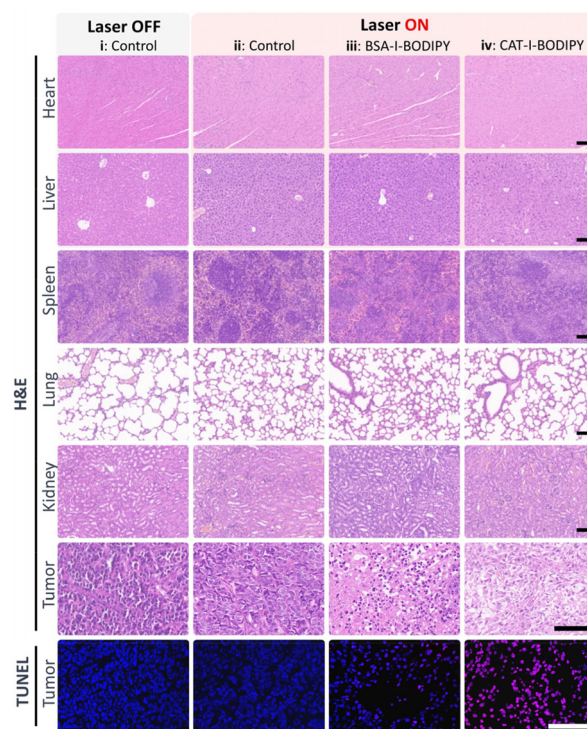
Fig. 7 H&E and TUNEL staining of tumour tissues and major organs from various treatment groups in nude mice. Scale bar: 100 μm.

3.9 *In vivo* biosafety evaluation

Evaluating the *in vivo* biosafety of CIB NPs incorporated a range of assessment metrics, including the monitoring of body weight fluctuations and histopathological examinations. Throughout the treatment period, body weight changes of mice across all experimental groups were routinely recorded (Fig. 6e). Our observations confirmed stable weight profiles with no irregular shifts, indicative of the overall tolerability and non-toxicity of the administered CIB NPs.

To augment these findings, histopathological investigations using Hematoxylin and Eosin (H&E) staining were performed on major organs in each experimental group (Fig. 7). These analyses enabled the direct visualization of any potential tissue damage or inflammation instigated by the CIB NPs. Notably, our examinations revealed no signs of cellular necrosis or inflammatory lesions, underscoring the promising safety profile of CIB NPs. Furthermore, the hemocompatibility test revealed that even at higher concentrations of CIB NPs, a very low hemolysis rate is maintained, underscoring the excellent biosafety of these NPs (Fig. S40†). Altogether, these observations collectively affirm the *in vivo* biosafety and biocompatibility of CIB NPs, bolstering their therapeutic potential in the context of cancer treatment. These reassuring findings lay a crucial foundation for advancing CIB NPs into further preclinical investigations and potentially, clinical trials.

4. Conclusions

In summary, this study presented a novel self-assembled bio-nanomaterial, CIB NPs, which offered a promising approach for imaging-guided enhanced PDT to hypoxic tumours. TEM and DLS well confirmed the successful construction of the nanoassemblies based on the hydrophilic protein and hydrophobic I-BODIPY. The assembled nanoprobe also retained its oxygen production capability, fluorescence imaging ability, and singlet oxygen generation capacity. Notably, it was observed that the nanoprobe reached maximum accumulation in the tumour site 18 h post-injection, providing a reliable basis for the implementation of precise PDT. *In vitro* and *in vivo* results on A549 demonstrated pronounced inhibition of tumour growth under NIR illumination due to the *in situ* supply of oxygen. Moreover, *in vivo* safety tests revealed favourable biocompatibility and negligible side effects in major organs, supporting the possible clinical application of CIB NPs in cancer treatment. This work will potentially pave the way for the development of more precise and effective diagnostic and therapeutic strategies in oncology, benefiting patients with hypoxic tumours.

Conflicts of interest

There are no conflicts to declare.

References

1 D. Peer, J. M. Karp, S. Hong, O. C. Farokhzad, R. Margalit and R. Langer, *Nat. Nanotechnol.*, 2007, **2**, 751–760.
2 E. Cybulla and A. Vindigni, *Nat. Rev. Cancer*, 2023, **23**, 6–24.
3 X. Zheng, W. Sun, M. Ju, J. Wu, H. Huang and B. Shen, *Biomater. Sci.*, 2022, **10**, 4681–4693.
4 D. Zhang, K. Teng, L. Zhao, L. Niu and Q. Yang, *Adv. Mater.*, 2023, e2209789.
5 B. Sun, R. Chang, S. Cao, C. Yuan, L. Zhao, H. Yang, J. Li, X. Yan and J. C. M. Hest, *Angew. Chem.*, 2020, **132**, 20763–20769.
6 B. Ji, M. Wei and B. Yang, *Theranostics*, 2022, **12**, 434–458.
7 J. Hu, Y. Tang, A. H. Elmenoufy, H. Xu, Z. Cheng and X. Yang, *Small*, 2015, **11**, 5860–5887.
8 B. M. Luby, C. D. Walsh and G. Zheng, *Angew. Chem., Int. Ed.*, 2019, **58**, 2558–2569.
9 L. Gai, Y. Liu, Z. Zhou, H. Lu and Z. Guo, *Coord. Chem. Rev.*, 2023, **481**, 215041.
10 Z. Mao, J. H. Kim, J. Lee, H. Xiong, F. Zhang and J. S. Kim, *Coord. Chem. Rev.*, 2023, **476**, 214908.
11 K.-X. Teng, L.-Y. Niu, Y.-F. Kang and Q.-Z. Yang, *Chem. Sci.*, 2020, **12**, 488–489.
12 A. Tabero, F. García-Garrido, A. Prieto-Castañeda, E. Palao, A. R. Agarrabeitia, I. García-Moreno, A. Villanueva, S. de la Moya and M. J. Ortiz, *Chem. Commun.*, 2019, **56**, 940–943.
13 K. Deng, C. Li, S. Huang, B. Xing, D. Jin, Q. Zeng, Z. Hou and J. Lin, *Small*, 2017, **13**, 1702299.
14 K.-X. Teng, L.-Y. Niu and Q.-Z. Yang, *J. Am. Chem. Soc.*, 2023, **145**, 4081–4087.
15 M. Zhao, Y. Xu, M. Xie, L. Zou, Z. Wang, S. Liu and Q. Zhao, *Adv. Healthcare Mater.*, 2018, **7**, 1800606.
16 J. Zou, Z. Yin, K. Ding, Q. Tang, J. Li, W. Si, J. Shao, Q. Zhang, W. Huang and X. Dong, *ACS Appl. Mater. Interfaces*, 2017, **9**, 32475–32481.
17 Y. Lai, Y. Dang, F. Li, C. Ding, H. Yu, W. Zhang and Z. Xu, *Adv. Funct. Mater.*, 2022, **32**, 2200016.
18 Q. Wang, J. Xu, R. Geng, J. Cai, J. Li, C. Xie, W. Tang, Q. Shen, W. Huang and Q. Fan, *Biomaterials*, 2020, **231**, 119671.
19 G. Lv, W. Guo, W. Zhang, T. Zhang, S. Li, S. Chen, A. S. Eltahan, D. Wang, Y. Wang, J. Zhang, P. C. Wang, J. Chang and X.-J. Liang, *ACS Nano*, 2016, **10**, 9637–9645.

20 X. Zhang, J. O. Machuki, W. Pan, W. Cai, Z. Xi, F. Shen, L. Zhang, Y. Yang, F. Gao and M. Guan, *ACS Nano*, 2020, **14**, 4045–4060.

21 X. Yin, Y. Cheng, Y. Feng, W. R. Stiles, S. H. Park, H. Kang and H. S. Choi, *Adv. Drug Delivery Rev.*, 2022, **189**, 114483.

22 J. Zheng, S.-H. Chen, B. Huang, M. Zhang, Q. Yuan and R. Cui, *Chin. Chem. Lett.*, 2023, 108460.

23 B. Tian, S. Liu, C. Yu, S. Liu, S. Dong, L. Feng, N. Hu and P. Yang, *Adv. Funct. Mater.*, 2023, **33**, 2300818.

24 N. Jiang, Z. Zhou, W. Xiong, J. Chen, J. Shen, R. Li and R. Ye, *Chin. Chem. Lett.*, 2021, **32**, 3948–3953.

25 Q. Ma, X. Sun, W. Wang, D. Yang, C. Yang, Q. Shen and J. Shao, *Chin. Chem. Lett.*, 2022, **33**, 1681–1692.

26 X. Guo, B. Tang, Q. Wu, W. Bu, F. Zhang, C. Yu, L. Jiao and E. Hao, *J. Mater. Chem. B*, 2022, **10**, 5612–5623.

27 M. Kolarikova, B. Hosikova, H. Dilenko, K. Barton-Tomankova, L. Valkova, R. Bajgar, L. Malina and H. Kolarova, *Med. Res. Rev.*, 2023, **43**, 717–774.

28 X. Li, S. Lee and J. Yoon, *Chem. Soc. Rev.*, 2018, **47**, 1174–1188.

29 L. Zhao, Y. Xing, R. Wang, F. Yu and F. Yu, *ACS Appl. Bio Mater.*, 2020, **3**, 86–106.

30 S. Li, Q. Zou, Y. Li, C. Yuan, R. Xing and X. Yan, *J. Am. Chem. Soc.*, 2018, **140**, 10794–10802.

31 H. Cheng, H. Dai, X. Tan, H. Li, H. Liang, C. Hu, M. Huang, J. Y. Lee, J. Zhao, L. Zhou, Y. Wang, L. Zhang and J. Yoon, *Adv. Mater.*, 2022, **34**, 2109111.

32 S. Qin, Y. Xu, H. Li, H. Chen and Z. Yuan, *Biomater. Sci.*, 2021, **10**, 51–84.

33 X. Li, N. Kwon, T. Guo, Z. Liu and J. Yoon, *Angew. Chem., Int. Ed.*, 2018, **57**, 11522–11531.

34 H. Wang, Y. Chao, J. Liu, W. Zhu, G. Wang, L. Xu and Z. Liu, *Biomaterials*, 2018, **181**, 310–317.

35 S. Z. F. Phua, G. Yang, W. Q. Lim, A. Verma, H. Chen, T. Thanabalu and Y. Zhao, *ACS Nano*, 2019, **13**, 4742–4751.

36 X. Cheng, L. He, J. Xu, Q. Fang, L. Yang, Y. Xue, X. Wang and R. Tang, *Acta Biomater.*, 2020, **112**, 234–249.

37 M. He, Z. Cheng, Z. Wang, M. Li, H. Liang, H. Liu, L. Yu, L. Zhao and F. Yu, *Adv. Healthcare Mater.*, 2023, e2300752.

38 N. Zhang, K. Mei, P. Guan, X. Hu and Y. Zhao, *Small*, 2020, **16**, 1907256.

39 L. Ding, X. Lin, Z. Lin, Y. Wu, X. Liu, J. Liu, M. Wu, X. Zhang and Y. Zeng, *ACS Appl. Mater. Interfaces*, 2020, **12**, 36906–36916.

40 J. Xie, Y. Wang, W. Choi, P. Jangili, Y. Ge, Y. Xu, J. Kang, L. Liu, B. Zhang, Z. Xie, J. He, N. Xie, G. Nie, H. Zhang and J. S. Kim, *Chem. Soc. Rev.*, 2021, **50**, 9152–9201.

41 L. Huang, J. Zhao, S. Guo, C. Zhang and J. Ma, *J. Org. Chem.*, 2013, **78**, 5627–5637.